Healing plasma current ramp-up by nitrogen seeding in the full tungsten environment of WEST

Patrick Maget, P Manas, J-F Artaud, C Bourdelle, J Bucalossi, H Bufferand, G Ciraolo, C Desgranges, P Devynck, R Dumont, et al.

Healing plasma current ramp-up by Nitrogen seeding in the full Tungsten environment of WEST

P. Maget, P. Manas, J-F Artaud, C. Bourdelle, J. Bucalossi, H. Bufferand, G. Ciraolo, C. Desgranges, P. Devynck, R. Dumont, N. Fedorczak, F. Felici[1], M. Goniche, C. Guillemaut, R. Guirlet, J. P. Gunn, T. Loarer, J. Morales, O. Sauter[1], S. Van Mulders[1], D. Vézinet, and the WEST team*

CEA, IRFM, F-13108 Saint Paul-lez-Durance, France.
[1] Ecole Polytechnique Fédérale de Lausanne (EPFL), Swiss Plasma Center (SPC), CH-1015 Lausanne, Switzerland
* see http://west.cea.fr/WESTteam

E-mail: patrick.maget@cea.fr

Abstract. Achieving a successful plasma current ramp-up in a full Tungsten tokamak can be challenging due to the large core radiation (and resulting low core temperature) that can be faced with this heavy metallic impurity if its relative concentration is too high. Nitrogen injection during the plasma current ramp-up of WEST discharges greatly improves core temperature and Magneto-Hydro-Dynamic stability. Experimental measurements and integrated simulations with the RAPTOR code complemented with the Qualikiz Neural Network for computing turbulent transport allow a detailed understanding of the mechanisms at play. Increased edge radiation during this transient phase is shown to improve confinement properties, driving higher core temperature and better MHD stability. This also leads to increased operation margins with respect to Tungsten contamination.

Submitted to: *Plasma Physics and Controlled Fusion*

1. Introduction

The injection of light impurities in tokamak plasmas appears a mandatory trade-off between maximizing potential fusion reactions in a pure Deuterium Tritium mix, and the preservation of plasma facing materials subject to erosion, contamination, recrystallisation and melting. By increasing plasma radiation in the edge region, light impurities help reducing plasma edge temperature and plasma facing material sputtering [1]. This issue is particularly critical in metallic devices where such sputtering releases heavy ions with a high radiation potential, leading to possible radiative collapse in the plasma core. For Tungsten in particular, the radiation peak around 1.5 keV constitutes a critical phase that must be passed through during the early plasma phase. As a

consequence, present metallic devices as well as a future fusion reactor require a well designed wall protection system including light impurity injection [2, 3].

The interest for light impurities is however not limited to high power, steady-state, phases, and it can be also profitable to the phase after plasma breakdown when the plasma current is ramped-up. This initial phase is indeed critical for plasma operation in terms of Magneto-Hydro-Dynamic (MHD) stability issues related with plasma contamination. In the early, low density plasma phase, some additionnal power systems cannot be used, such as RF necessitating sufficient density in front of the antennas (LHCD and ICRH), or Neutral Beam Injection (NBI) necessitating enough density to avoid shine-through. Only ECRH is an appropriate heating scheme in such early phases, as shown in ASDEX Upgrade [4], but it is not available in tokamaks like JET or WEST, leaving the ohmic current and density waveforms as the only possible actuators for mastering the power balance and MHD activity. In a series of experiments addressing the effect of high-Z limiters on FTU, the formation of hollow temperature profiles and radiative collapse was avoided by a strong gas puff or by the injection of Neon [5]. The evolution of the plasma current density towards a hollow shape in this context is also prone to trigger large MHD modes, in particular Double-Tearing Modes (DTM) [6, 7]. Although DTM crashes do facilitate current penetration during the ramp-up [8] and remove impurities radiating in the core, the lack of control on the triggering and consequences of this crash does not work in favor of this technique.

These issues related to plasma ramp-up were encountered in the WEST tokamak. This superconducting tokamak equipped with Tungsten plasma-facing components in divertor and main chamber [9] has been regularly facing low core electron temperature and the development of low frequency MHD activity, leading to a high level of disruptivity when Lower Hybrid heating was finally applied. The injection of Nitrogen during the first few seconds of plasma, during the rise of the plasma current, led to a significant increase of the core temperature, a peaking of the plasma current, and the avoidance of deleterious MHD activity. The regular use of this technique allowed identifying a number of characteristic signatures, and to draw schematically the domain where Nitrogen injection can be beneficial for obtaining a reliable plasma ramp-up phase.

Several aspects shall be considered while evaluating the benefit of light impurity injection in these experiments, as in steady-state phases. First, one has to evaluate the impact on turbulent transport. Indeed, light impurity injection often leads to an improvement of energy confinement [10, 11, 12, 13] thanks to the dilution of the main plasma ions and to the reduction of Ion Temperature Gradient driven transport [14, 15, 16]. The situation is more complicated in H-mode where impurity seeding does not solve the issue of wall erosion during Edge Localized Modes [17, 18, 19, 14]. Even in L-mode, there are however some drawbacks to the presence of light impurities in the plasma edge region. Due to their higher mass than the main plasma ion species, and their comparable temperature, these ions are prone to enhance the sputtering of plasma-facing components if their cooling effect is not strong enough to fall below the sputtering threshold energy [20, 21]. This issue of sputtering also applies when the

mass of the main ion species is increased, as demonstrated on JET for example when varying the Hydrogen/Deuterium fraction, which anticipates experiments with a mixed Deuterium/Tritium content [22]. The formation of Ammonia is also an issue to be considered when Nitrogen is to be used in a regular way [23, 24, 25, 26]. Evaluating how these beneficial and deleterious effects balance in the ramp-up experiments of WEST gives indications about the possible extension of Nitrogen seeding to future experiments.

In the present paper, we first describe the experiments performed on WEST in section 2, and we then characterize the effect of Nitrogen seeding on the ramp-up phase in section 3, showing the transient plasma detachment and the reduction of Tungsten sputtering on the lower divertor. Integrated simulations of the plasma evolution inside the Last Closed Flux Surface (LCFS) with the RAPTOR code [27, 28], described in section 4, allow evidencing the current peaking and the associated improvement of the confinement as the dominant mechanism. These simulations also demonstrate the increased scenario robustness towards plasma contamination by Tungsten ions that is obtained by early Nitrogen seeding.

2. Description of the experiment

The analysis of Nitrogen seeding effect in the plasma ramp-up phase on WEST is based on three series of consecutive pulses (21 pulses in total) from the 2019 experimental campaign where the quantity of Nitrogen injected in the plasma was varied. In these plasma discharges with Deuterium as the main ion species, the magnetic field was $B_0 = 3.7$T, and the plasma current ramps first to 300kA and then to 500kA, as shown in figure 1. The X-point is formed around $t = 1.5$s above the lower divertor. Nitrogen is injected from the outer limiter, starting at the plasma breakdown up to $t = 3.5$s (12 pulses) and $t = 4$s (9 pulses). In the following, we choose to represent the impact of Nitrogen seeding on the scenario as a function of the quantity of Nitrogen injected before the time considered, expressed in Pa.m^3. This choice is motivated by the persistence of the initial effect of the seeding on longer times, as evidenced on figure 1 for example. At $t = 4$s, the preforming phase ends, and RF power is injected, as evidenced by the increase of core temperature in figure 1. The plasma scenario is expected to be reproducible at this stage, and the role of the preforming phase is to ensure that, whatever happens in the very early phase of the plasma (at breakdown or at the X-point formation), plasma parameters can be controlled at the beginning of the main heating phase.

The effect of Nitrogen seeding will be analyzed using Electron Cyclotron Emission (ECE) for electron temperature measurements [29], neutron flux as a proxy for ion temperature, and interferometry for electron density. Note that during the 2019 experimental campaign, electron temperature measurements were found to be abnormally low by about a factor of two, for reasons that are still under investigation. In the meantime, a correction of these measurements has been applied, based on similar discharges performed in the former WEST experimental campaign where the consistency between ECE data, spectroscopic data and global energy content was assessed. The

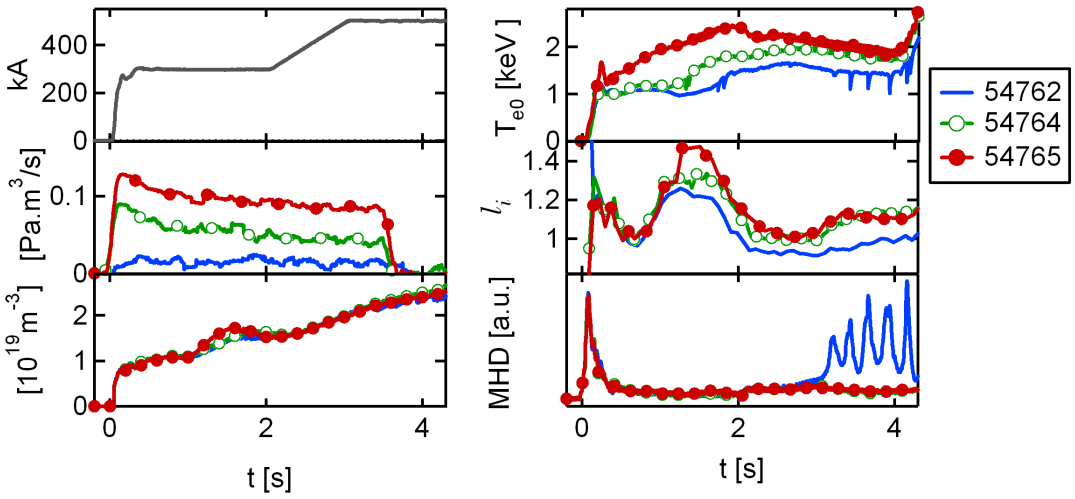

Figure 1. Example of 3 consecutive pulses (54762, 54764, 54765) with increasing Nitrogen seeding rate. Left column: plasma current (top), Nitrogen injection rate (middle) and volume averaged plasma density (bottom). Right column: central electron temperature, internal inductance and MHD level.

radiative power losses are evaluated using a 16 cords horizontal Bolometry system with two wide angle cameras located in a horizontal port and covering the whole plasma cross-section [30]. The separation between the bulk and SOL contributions to the total radiated power is obtained by an ad-hoc combination of core and edge bolometry channels that has been validated by synthetic data, giving a maximum error of about 20% [31]. The visible spectroscopy system covers the lower divertor with a radial resolution of about 1 cm in the two strike point regions [32], and UV spectroscopy [33] will be used for evidencing Nitrogen penetration into the plasma. The lower divertor is also equipped with Langmuir probes having a radial resolution of 1.2cm [34]. Finally, the magnetic equilibrium is reconstructed using the NICE code constrained by 10 polarimetry chords [35].

An example is shown in figure 1, with three consecutive plasma discharges where the Nitrogen gas valve is opened from the breakdown to about 3.5s, with a rate ranging from nearly zero to about 0.2 Pa.m^3/s. As the Nitrogen flow rate is increased, the core temperature rises, as well as the internal inductance, during the first plasma current plateau at 300 kA. The impact is less pronounced when reaching the current flat top at 500 kA, but a large Magneto-Hydro-Dynamics activity, starting around $t = 3$s on the discharge with nearly zero Nitrogen injection, is avoided in the discharges with N-seeding.

The improvement of the core temperature is illustrated in figure 2 where the profiles are shown at $t = 2$s for the same series of pulses (the plasma center is around $R = 2.45m$). The electron temperature is increased in the core plasma only, while the profile outside $R \sim 2.7m$ is left unchanged.

The tangential camera viewing the plasma from a mid-plane port in the visible range

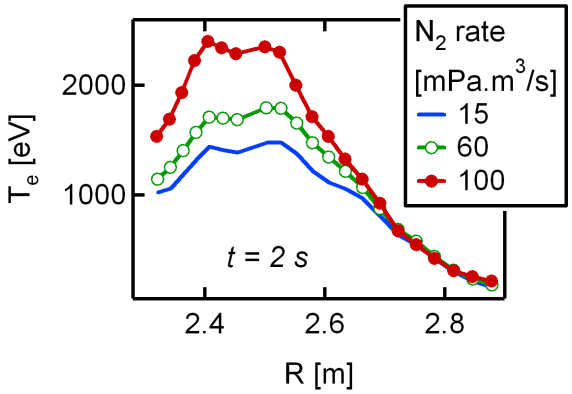

Figure 2. Electron temperature profiles at $t = 2$s for the three discharges of figure 1.

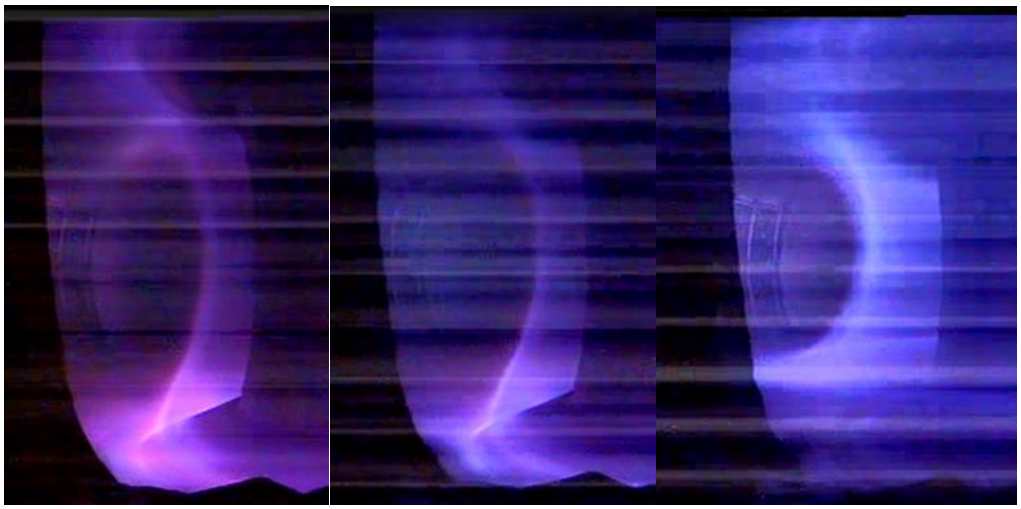

Figure 3. Tangential view in the visible range for three different N_2 injection rates, at $t = 2$s: 0 (55797, left), 0.13 (55799, middle) and 0.14 (55800, right) Pa.m^3/s.

evidences a modification of the radiation pattern when Nitrogen is injected (figure 3, from other pulses than those shown in previous figures), with a visible emission that evolves from pink to blue. At large injection levels (right plot), the radiative layer moves well inside the plasma separatrix, and starts to be associated with a growing MHD activity.

3. Confinement and scenario issue

3.1. Global parameters from experimental database

The impact of Nitrogen seeding is documented by recording relevant plasma parameters at $t = 2$s and $t = 3$s (end of first plateau at 300 kA and beginning of main plateau at 500 kA), from the database of 21 pulses. We show in figure 4 the central temperature, internal inductance, volume averaged density, density peaking, energy content, resistive Z_{eff}, loop voltage and neutron rate, as a function of the level of Nitrogen injected up to these two times (i.e. the time integral of the Nitrogen injection rate up to these two times). The resistive Z_{eff} is computed so as to match the flux consumption in the ohmic phase of the discharge. Quantities are averaged over 200ms, and the standard deviation gives the error bars. For one of the series, the density at $t = 3$s is significantly larger than for the others, and we will identify these points with a bold contour in the following plots.

The effect of N-seeding at $t = 2$s appears to be robust. The core temperature increases quasi-linearly by about a factor of two up to a Nitrogen injection rate of about 0.1 Pa.m$^3/s$, the internal inductance increases by about 30%, indicating a peaking of the current profile. The plasma energy content (W_{MHD}) is increased by about 50%, and the neutron rate is also largely improved, suggesting that ion temperature also benefits from N-seeding. A noticeable improvement in the flux consumption is also recorded with a significant decrease of the loop voltage and a resistive Z_{eff} that is stable. This indicates that Nitrogen contamination is small enough to let the temperature increase dominate over Z_{eff} in the plasma resistivity modification, since plasma resistivity varies as $Z_{eff}/T^{3/2}$. The effect of N-seeding on the current profile peaking (characterized by the internal inductance) is less pronounced at the end of the plasma ramp-up ($t = 3$s), but it is maintained qualitatively on all the parameters shown in the figure. Finally, the density peaking increases notably at $t = 2$s while increasing Nitrogen seeding, but this effect vanishes at $t = 3$s. Note that the series with a larger density at that time behaves similarly, except for the core temperature for which the increase with Nitrogen injection is slightly reduced.

The variation of injected (ohmic) and radiated powers is shown in figure 5. Following the decrease of the loop voltage, the ohmic power injected into the plasma is found to decrease slightly as more Nitrogen is injected. The radiative loss shows a moderate increase that is attributed to the bulk plasma contribution, while the power radiated in the Scrape-off Layer (SOL) tends to decrease. These variations will be exploited to constrain integrated simulation settings described later. The series with a larger density at $t = 3$s has a similar total radiated power, but the fraction coming from the SOL is larger.

In this database however, the pulse where the level of Nitrogen is the highest shows a lower performance at $t = 2$s (the loop voltage at $t = 2$s is around 2.8V, out of the scale of the figure). In this pulse, a large MHD activity has developed around $t = 1s$ and lasts until $t \sim 2.2s$, when it completely disappears. The analysis of Mirnov coil

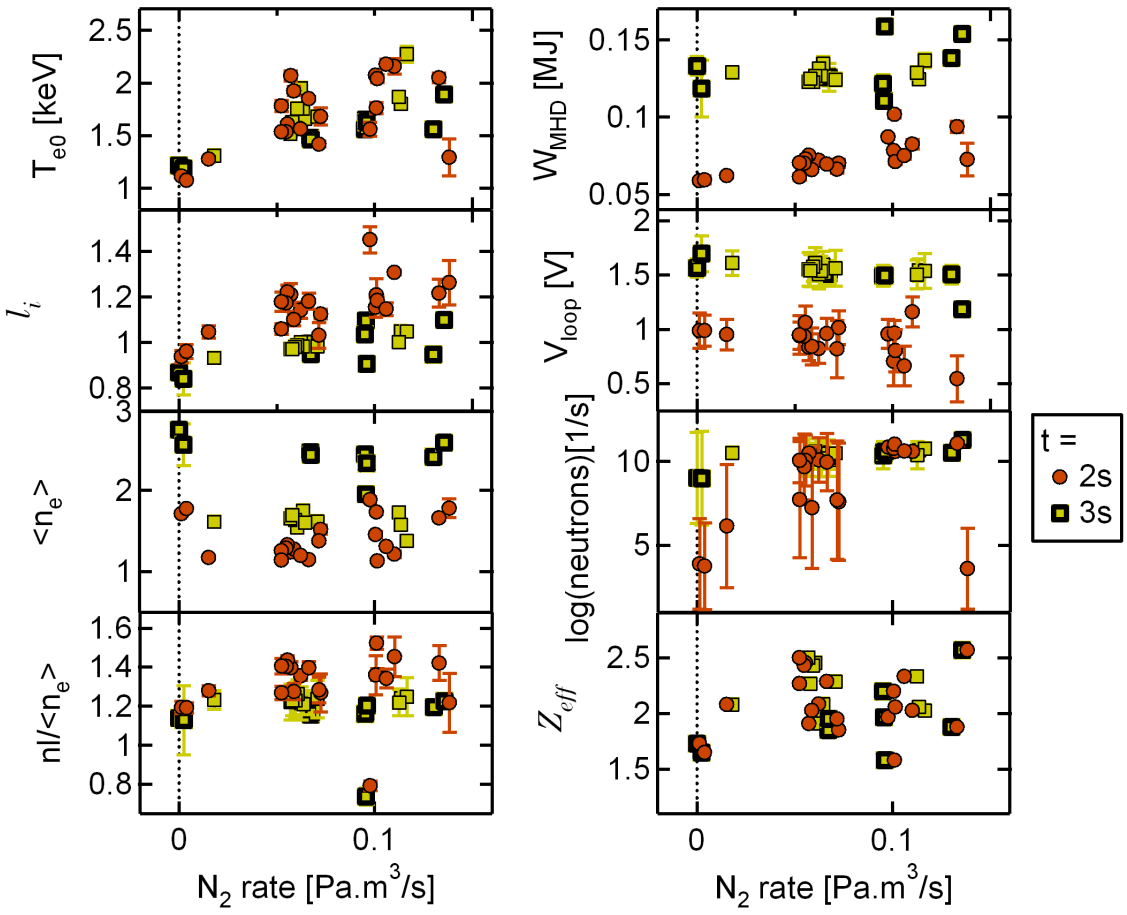

Figure 4. Central electron temperature, internal inductance, volume averaged density, density peaking, energy content, loop voltage, neutron rate and resistive Z_{eff}, at $t = 2$s and $t = 3$s as a function of the Nitrogen injection rate. Bold symbols correspond to the series with a higher density at $t = 3$s.

data shows that this MHD mode has a toroidal mode number $n = 1$ and poloidal components $m = 2$, 3. During the 2019 campaign, a similar behavior was observed several times, and sometimes ended with a disruption. A reliable recipe was then to decrease the level of Nitrogen, thus indicating that the range where Nitrogen injection can be varied during this early plasma phase is limited. The power balance (between ohmic power and power radiated inside the confined plasma) explains this limitation by the proximity to a radiative collapse. This is evidenced in figure 6: when Nitrogen is injected, the radiative fraction can become large and approach unity. As this limit is approached, the position of the radiative layer in the visible range showed in figure 3 moves deeply inwards, producing sometimes a disruption, and thus setting an upper limit to the favorable Nitrogen injection rate.

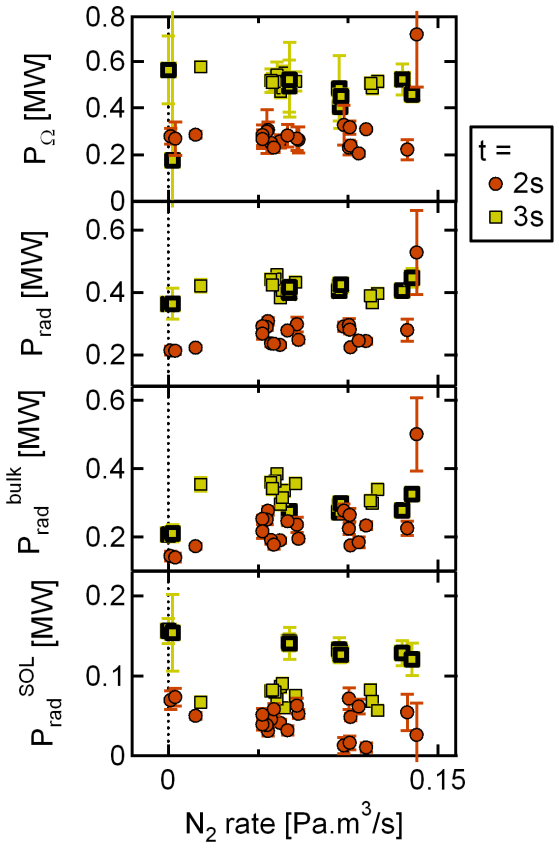

Figure 5. From top to bottom: ohmic power, total, bulk and SOL radiated powers at $t = 2$s and $t = 3$s as a function of the Nitrogen injection rate. Bold symbols correspond to the series with a higher density at $t = 3$s.

3.2. Divertor detachment

Nitrogen injection in the early phase of the discharge, where the power crossing the separatrix is low, generates a plasma detachment on WEST, as evidenced by Langmuir probe measurements on the lower divertor. This results from the fact that a large fraction of the power entering the SOL is radiated instead of being transferred onto the divertor [36]. We show in figure 7 the temperature profile during the detached phase and just after the re-attachment for two of the pulse series where Nitrogen is injected up to $t = 3.5$s and $t = 4$s (measurements are not available for the other series). During detachment, the measured electron temperature at both the inner and outer strike points (ISP and OSP respectively) is around 5 eV, while it increases to around 30 eV on the outer strike point (30 to 40 eV on the inner one) after the plasma reattaches.

A clear correlation is found between the duration of the detached phase and the Nitrogen injection rate, as shown in figure 8. At $t = 3$s, when the plasma reaches the current plateau of 500kA, the detached phase is ended in all these cases due to reduced fraction of Ohmic power radiated in the core, as shown in figure 6.

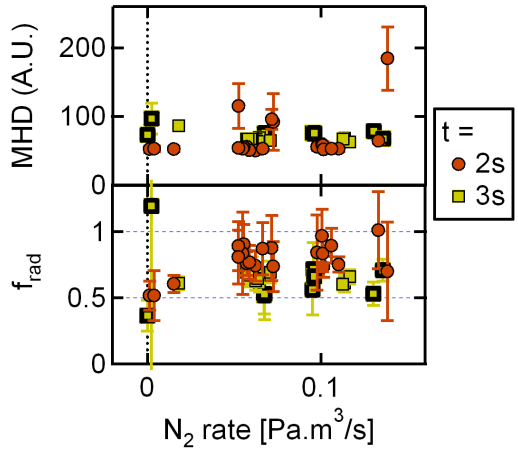

Figure 6. MHD activity recorded by Mirnov coils (top) and radiative fraction P^{bulk}/P_{Ω} (bottom), at $t = 2$s and $t = 3$s as a function of the Nitrogen injection rate. Bold symbols correspond to the series with a higher density at $t = 3$s.

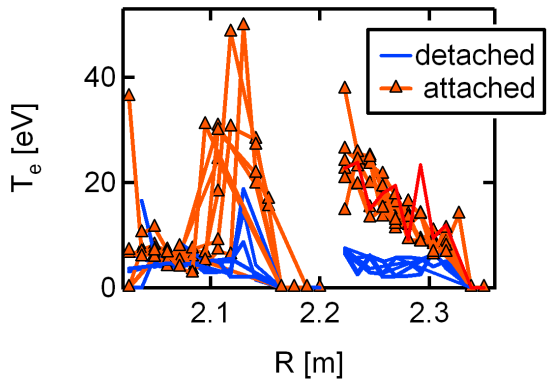

Figure 7. Electron temperature profile at the lower divertor measured with Langmuir probes during and after the detached phase.

3.3. Nitrogen penetration and Tungsten sputtering

The presence of Nitrogen in the plasma edge is evaluated by measuring the brightness of the Nitrogen II line at 399.5nm in the lower divertor region. Normalizing it to the brightness of the Deuterium I line at 434.1nm (D_γ) allows quantifying its relative concentration. Figure 9 (top plot) shows this normalized quantity as a function of the Nitrogen injected up to $t = 2$s and $t = 3$s. The diffusion of Nitrogen deeper inside the plasma is attested by the increase of the Nitrogen VII line (normalized to plasma density) from UV spectroscopy (bottom plot).

The Tungsten sputtering on the lower divertor is evaluated by considering the brightness of the WI line at 400.9nm, normalized by the DI line brightness at 434.1nm. This quantity is calculated for the line of sight which measures the highest D_γ brightness

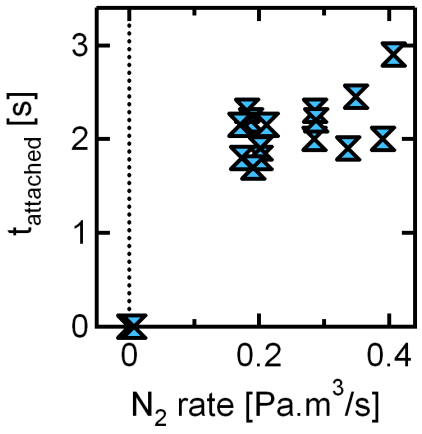

Figure 8. Time when the plasma reattaches as a function of the Nitrogen injection rate.

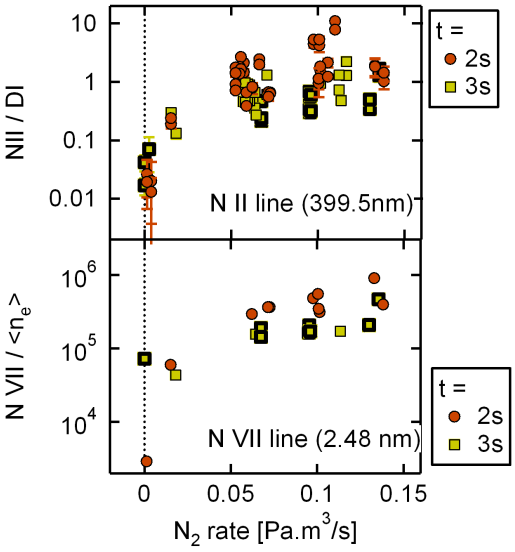

Figure 9. Top: Emission of the Nitrogen II line at 399.5nm normalized to the Deuterium I line at 434.1nm measured at the inner and outer strike points, at $t = 2$s and $t = 3$s as a function of the Nitrogen injection rate. Bottom: emission of the Nitrogen VII line at $t = 2$s and $t = 3$s as a function of the Nitrogen injection rate. Bold symbols correspond to the series with a higher density at $t = 3$s.

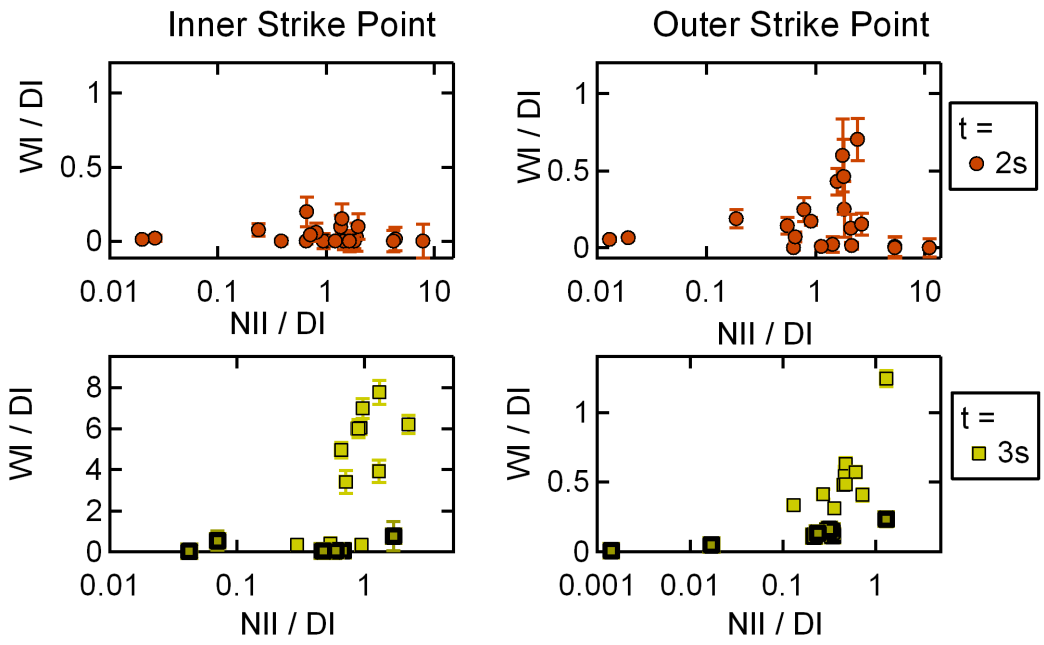

Figure 10. Emission of the Tungsten I line at 400.9nm normalized to the D_γ (434.1nm) brightness on the inner (left plots) and outer (right plots) strike points, as a function of the normalized Nitrogen II line at 399.5nm, at $t = 2$s (top) and $t = 3$s (bottom plots). Bold symbols correspond to the series with a higher density at $t = 3$s.

on the inner and outer strike points, located on the lower divertor. The result is plotted in figure 10 as a function of the normalized brightness of the NII line, which is representative of the quantity of Nitrogen present close to the divertor surface. At $t = 2$s, Tungsten sputtering at the Inner (ISP) and Outer (OSP) Strike Points is low. This is consistent with plasma conditions close to detachment at this time.

At $t = 3$s, after the plasma has re-attached, Tungsten sputtering increases strongly with the Nitrogen seeding, particularly at the ISP where the ratio WI/DI reaches values that are about one order of magnitude larger than at the OSP. The absolute level of the sputtering is however reduced for the series with the larger electron density (bold symbols). These measurement indicate that Nitrogen ions contribute to the sputtering at the end of the preforming phase.

But for evaluating the overall impact of Nitrogen seeding technique during the ramp-up of the plasma current, it is important to consider the question of the plasma contamination measured after this transitory phase rather than the sputtering on the divertor, given the fact that prompt redeposition significantly impact the quantity of Tungsten atoms going to the confined plasma [37].

3.4. Impurity contamination

We now focus on the role of Nitrogen seeding in the plasma contamination by Tungsten and Nitrogen. Bolometry inversion is used to reconstruct the profile of radiative power losses, with the plasma radius divided into 6 shells, and radiative power density is assumed to be homogeneous on flux surfaces in the confined plasma. The radiative power density at plasma center and at $r/a = 0.8$ is plotted in figure 11 as a function of the quantity of Nitrogen injected before $t = 3$s, when the current flat top is reached: this is when we want to evaluate the impact of N_2 seeding on plasma contamination. In the plasma core, there is no correlation between Nitrogen injection and the core radiation. The relative concentration of Tungsten in the plasma core can be estimated from the radiative losses, and it is in the range $[0.5,\ 2] \times 10^{-4}$. The series with a larger electron density (bold symbols) has a lower Tungsten concentration, but we do not see any significant change of this core contamination as the quantity of Nitrogen is increased. As we approach the edge region, radiative losses increase regularly with the quantity of Nitrogen that is injected. This increase is consistent with an increased concentration of Nitrogen in the edge region (see next section). From bolometer measurements, we do not see therefore any indication that Nitrogen seeding changes the core contamination by Tungsten after the current ramp-up phase, but we do infer a lower concentration in the series that has a larger density.

4. Integrated modelling

The impact of Nitrogen seeding on the discharge evolution is investigated with the RAPTOR code [27, 28], with transport coefficients computed using the quasilinear gyrokinetic code Qualikiz [38] for which a 10D Neural Network version (QLKNN) [39] has been coupled to RAPTOR [40]. Radiative losses coming from Nitrogen and Tungsten species are taken into account using effective collisional-radiative coefficients from the ADAS database [41]. In particular this work makes use of the W coefficients from [42]. The Nitrogen concentration is deduced from a prescribed Z_{eff} profile, and the Tungsten density is taken proportional to that of electrons, with a concentration assumed to be low enough not to contribute to electroneutrality. The Porcelli sawtooth model [43] implemented in RAPTOR is used to prevent the safety factor to go far below unity as plasma current diffuses [44]. This plays an important role here due to the contribution of core ohmic current in the mechanism at play. We do not compute particle transport in these simulations. By doing this, we ignore the effect of Nitrogen seeding on density peaking that was observed in the database at $t = 2$s (see figure 4). We will come back on this aspect in the discussion (section 5).

The plasma current and density evolution is taken from one of the discharges of the database (pulse 55797) without Nitrogen injection. The simulation is started at $t = 0.5s$ up to $t = 4s$. This pulse belongs to the series with higher density at $t = 3$s, and as shown in figure 11, the Tungsten concentration is $c_W \approx 10^{-4}$. In order to check the validity of

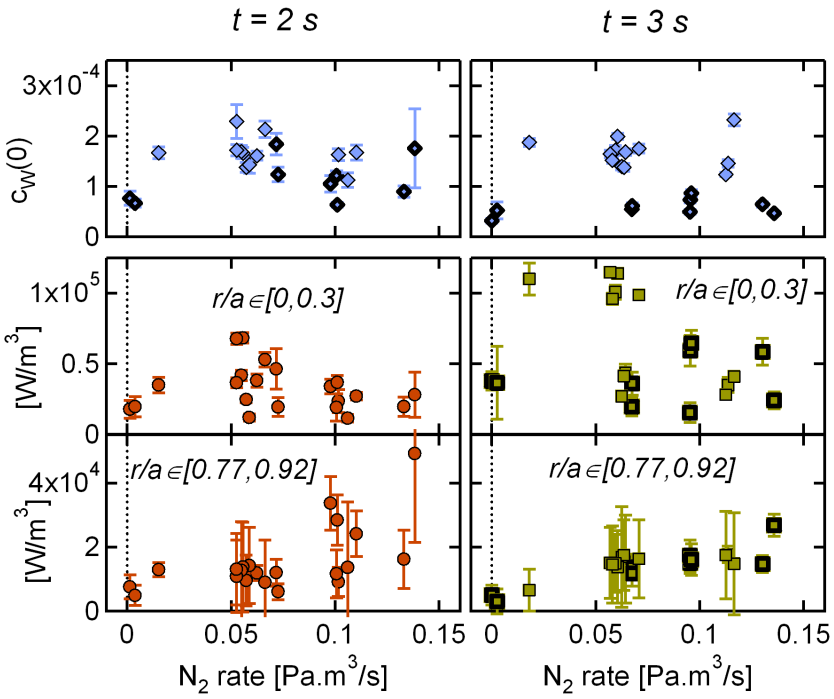

Figure 11. Bolometry inversion: from top to bottom, Tungsten concentration deduced from core radiation, radiative power emission in the core region and in the edge region, as a function of the Nitrogen injection rate at $t = 2$s (left column) and $t = 3$s (right column). Bold symbols correspond to the series with a higher density at $t = 3$s.

the QLKNN model in the early plasma phase of WEST discharges, the prediction of the core temperature for a flat Z_{eff} profile using RAPTOR/QLKNN has been compared to a similar integrated simulation using ASTRA [45] coupled to Qualikiz, and ASTRA coupled to the gyrofluid code TGLF [46] (figure 12). The good agreement obtained is expected in this case where ITG are dominant, as confirmed by the computation of turbulent modes at mid-radius with the gyro-kinetic code GKW [47] showing the predominance of ITG modes. Note that the QuaLiKiz collision Krook operator has been recently upgraded and a revised QLKNN is being prepared for covering the case of TEM dominated regimes.This extensive comparison gives confidence that the QLKNN model is appropriate for simulating the current ramp-up phase of WEST discharges.

In the simulations to be presented, we will focus on the profiles obtained at $t = 2s$, and several simulation settings have been constrained on the experimental observations. These settings are the simulation boundary, the reference Z_{eff} profile without Nitrogen seeding, and the Z_{eff} profile shape. The choices that have been made are illustrated in figures 13 and 14. In the very edge of the plasma, the QLKNN model underestimates the heat diffusivity and predicts temperature gradients that are too large compared to what is observed (figure 13). This is possibly due to resistive modes that are not taken into account in the model, or to Trapped Electron Modes (TEM) whose impact on turbulent transport is underestimated in the Neural Network version QLKNN that is used here.

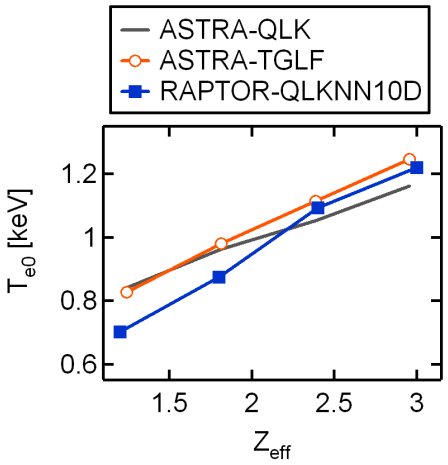

Figure 12. Central electron temperature predicted by ASTRA-QLK, ASTRA-TGLF and RAPTOR-QLKNN, as a function of Z_{eff} (a flat profile is assumed).

We had to impose a boundary condition at $r/a = 0.8$ for the temperature prediction in order to recover temperature profiles consistent with experimental measurements, with the cost of loosing a predictive modeling of this quantity in the edge region.

The second parameter is the background Z_{eff}. As shown in figure 13, the temperature profile is significantly more peaked when the background Z_{eff} is increased, and taking a value close to the resistive value $Z_{eff} \approx 2$ deduced from the flux consumption yields a good agreement with the experimental profile, not only close to the boundary, but also in the core. This outlines the strong dependence of core profiles on edge conditions. By assuming that the intrinsic light impurity is Nitrogen, we make of course a simplification of the experimental situation, the real mixture including in fact Oxygen and Carbon as other contributors.

One of the constraints is also to reproduce in the RAPTOR simulations the slight decrease of the ohmic power as more Nitrogen is injected (see figure 5). It has to be noted that by choosing a boundary at $r/a = 0.8$ we do not take into account the changes in temperature due to different radiation levels between this boundary and the plasma separatrix. We note that this change is however limited in the range of Nitrogen seeding that is used in the experiment (see later). When taking a flat Z_{eff} profile, we do obtain an increase of the core temperature but the ohmic power also increases, as well as the loop voltage shown in figure 14. With a Z_{eff} that increases linearly or quadratically with the plasma radius (the edge value is given at $r/a = 1$), the Ohmic power decreases with Z_{eff}^{edge}, because the gain in electric conductivity from the increased temperature is larger than the loss due to the higher effective charge of the plasma. This kind of dependence seems therefore the most appropriate for describing the ramp-up phase in the WEST discharges. Note that the limitation of the core temperature seen for example for the linear Z_{eff} profile for Z_{eff}^{edge} above 3.5 is due to the sawtooth activity being active as the current profile peaks. In the following, we will adopt a parabolic profile, with a core value $Z_{eff}(0) = 2$.

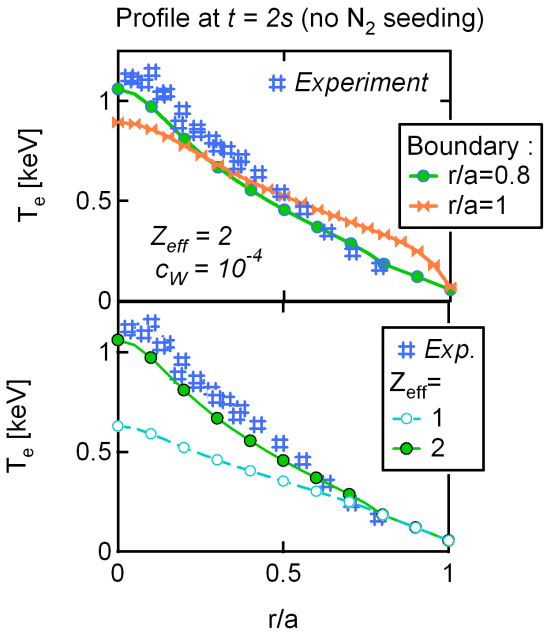

Figure 13. Top : Experimental and simulated electron temperature profiles at $t = 2s$ for a boundary condition at $r/a = 1$ and $r/a = 0.8$ for a non-seeded case (flat $Z_{eff} = 2$, $c_W = 10^{-4}$). Below: effect of background light impurity content.

The electron temperature profiles obtained at $t = 2s$ for the series following pulse 55797 are shown in figure 15. As for the example shown in figure 2, the beneficial effect of Nitrogen injection translates into an increase of the electron temperature in the core region, while we see a limited impact outside $r/a = 0.7$. For this pulse series, the upper limit is for 1.4 Pa.m^3/s, a level at which the discharge enters a highly detached regime with strong MHD activity (see figure 3, right plot). Electron temperature profiles obtained in the integrated simulations are shown for $Z_{eff}^{edge} = 2$ (no Nitrogen seeding) and for $Z_{eff}^{edge} = 6$ on the same plot. Nitrogen seeding effect is well reproduced, although the gain in temperature is underestimated by about 25% in the core. The sensitivity to the exact shape of the Z_{eff} profile and to the core Z_{eff} value, both illustrated in figure 13 and 14, could well explain this level of disagreement.

Experiment and simulation can be compared over several key observables such as the core temperature, internal inductance, loop voltage, ohmic power, radiated power and radiative fraction, once a correspondence between the Z_{eff} and the mean injection rate is found. We find that taking the following relation:

$$Z_{eff}^{edge} = 100/3 N_{2[Pa.m^3/s]}^{rate} + 2 \qquad (1)$$

allows a fairly good match on these key parameters, as shown in figure 16 where we compare the database described in section 3.1 with the scan in Z_{eff}^{edge} performed from a reference pulse without seeding. A Tungsten concentration in between 10^{-4} and 2×10^{-4}, consistent with the bolometry inversion shown in figure 11, provide a good quantitative agreement with the experiments.

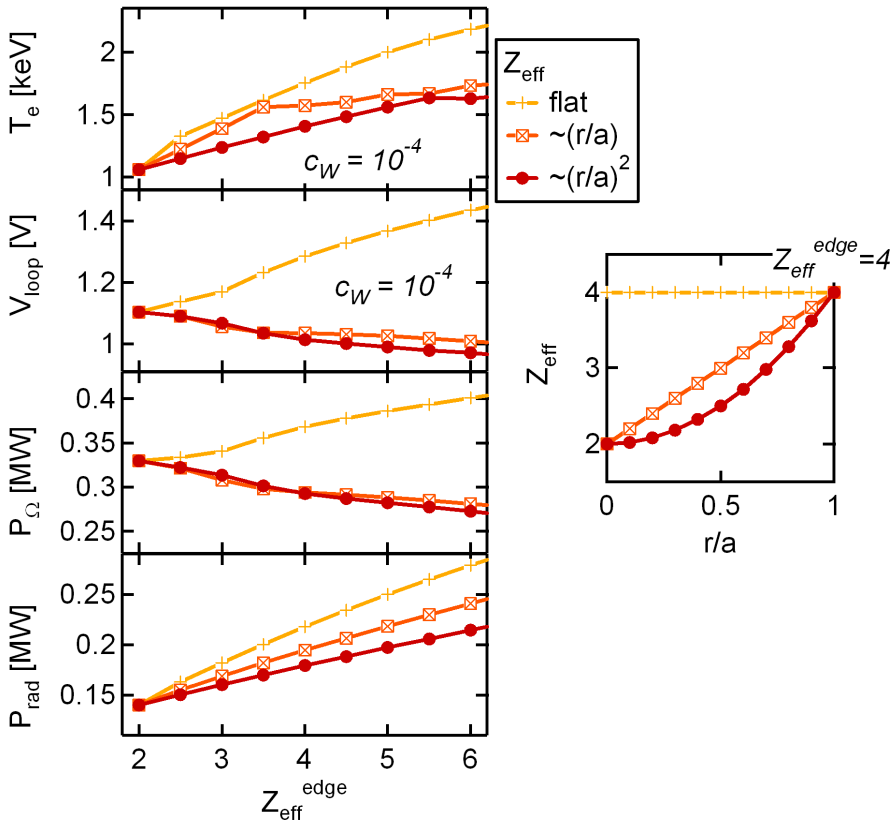

Figure 14. RAPTOR simulations, from top to bottom: central electron temperature, loop voltage, ohmic power and radiated power at $t = 2$s as a function of the edge Z_{eff} for a flat profile, and for profiles varying as (r/a) and $(r/a)^2$ (case with $c_W = 10^{-4}$, $Z_{eff}(0) = 2$). An example of the corresponding Z_{eff} profiles is shown in the right plot for $Z_{eff}^{edge} = 4$.

The value of the central safety factor at $t = 2s$ as a function of the edge Z_{eff} is shown in figure 17. It evidences the faster current diffusion that is achieved as more Nitrogen is injected. The time of the first sawtooth is therefore another criterion that can be used to compare integrated simulations with experimental observations. This time is plotted in figure 18 against the Z_{eff}^{edge} for the simulation part, and as a function of the Nitrogen injection rate averaged over 3s for pulses series where this injection lasts more than 3s (i.e. 3 pulse series over 4). The time is set at 4s when no sawtooth regime is detected during the preforming phase covered by the simulations. In practice, the detection of the first sawtooth is often difficult in the experiment, where we can have isolated crashes that look like sawteeth but does not mark the start of a regular sawtooth regime. They could correspond to either real sawteeth initiating a more complex reorganization of the current profile in the core, or to Double-Tearing Modes at $q > 1$. The series shown in figure 1 has a very clear transition to a sawtooth regime, and is refereed to as S1 in figure 18. The series S2 is also globally consistent with the integrated simulation results,

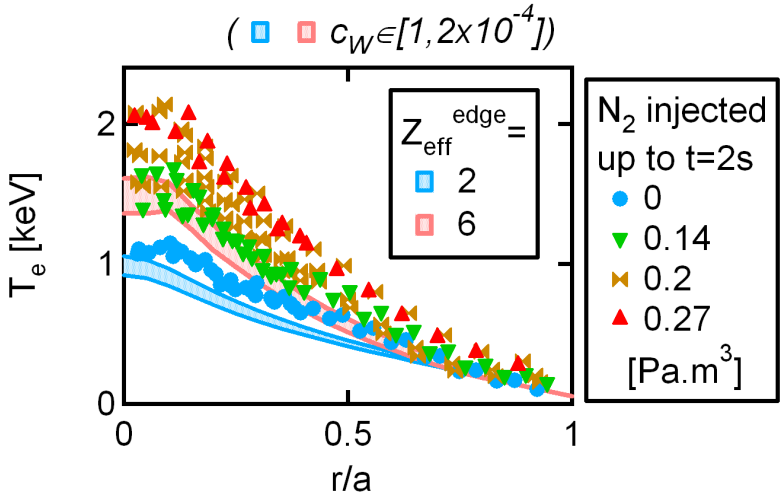

Figure 15. Electron temperature profile from the reference pulse without Nitrogen seeding (55797) and the following pulses with increasing levels of Nitrogen injection, compared to RAPTOR simulations with $Z_{eff}^{edge} = 2$ and $Z_{eff}^{edge} = 6$, at $t = 2$s, for Tungsten concentration between 10^{-4} and 2×10^{-4}.

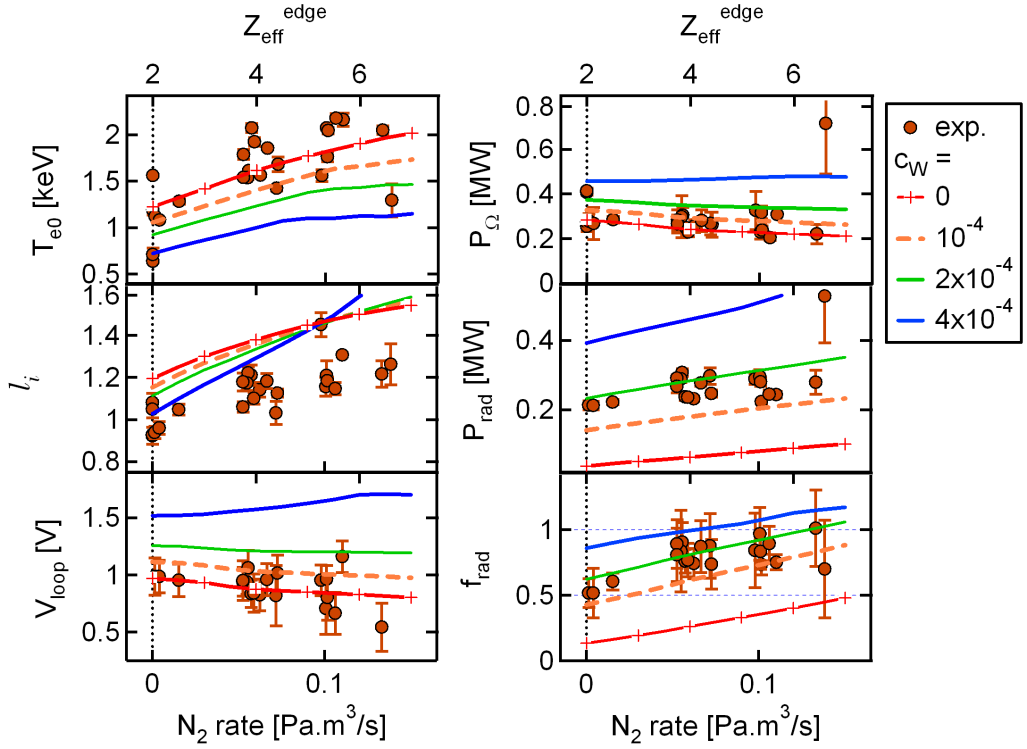

Figure 16. Core electron temperature, internal inductance, loop voltage, ohmic power, radiated power and radiated power fraction at $t = 2s$ as a function of N_2 injection rate for experimental data, and of Z_{eff}^{edge} for simulation data, with different levels of Tungsten concentration.

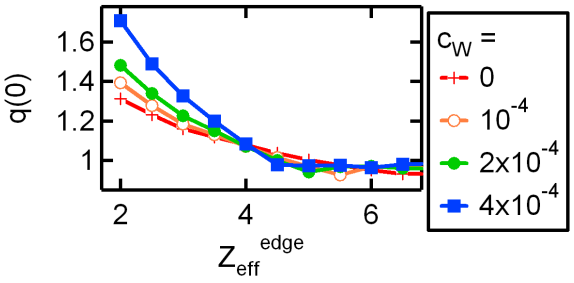

Figure 17. Central safety factor value at $t = 2s$ as a function the edge Z_{eff}, for different levels of Tungsten concentration.

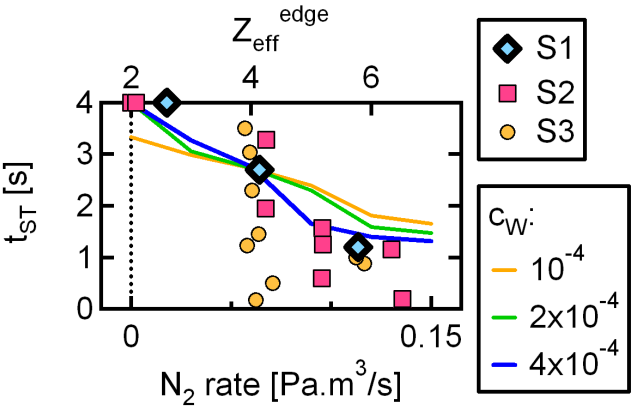

Figure 18. Time of appearance of sawtooth regime as a function of the N2 injection rate for experimental data (S1, S2 and S3 are three of the four series of pulses included in the database), and of Z_{eff}^{edge} for simulation data with different levels of Tungsten concentration.

while the behavior of the series noted as S3 in figure 18 is generally inconsistent on this particular sawtooth criterion, possibly hiding complex core plasma evolution that do not impact less sensitive parameters like the ones shown in figure 16.

The time evolution of the central electron temperature without Tungsten, and for a relative Tungsten concentration of 10^{-4} and 6×10^{-4}, is shown in figure 19 for different values of the edge Z_{eff}. The total plasma current and central electron density that are both prescribed in the simulation are also shown in the figure. The presence of Nitrogen in the edge region is shown to increase the core electron temperature, and this increase improves the tolerance to the presence of Tungsten, as demonstrated for the extreme case with a relative fraction of Tungsten $c_W = 6 \times 10^{-4}$, by preventing a radiative collapse.

Several mechanisms are at play when Nitrogen seeding is used. They can be evaluated by considering i) the normalized temperature gradient R/L_{Te}, and ii) the net heat source, i.e. the difference between the ohmic heat source and the radiated power. As shown in figure 20 for a Tungsten concentration consistent with that of the experiments, the net power density is barely changed in the plasma core ($r/a < 0.2$), while it goes to slightly negative values in the edge region due to the increased Nitrogen

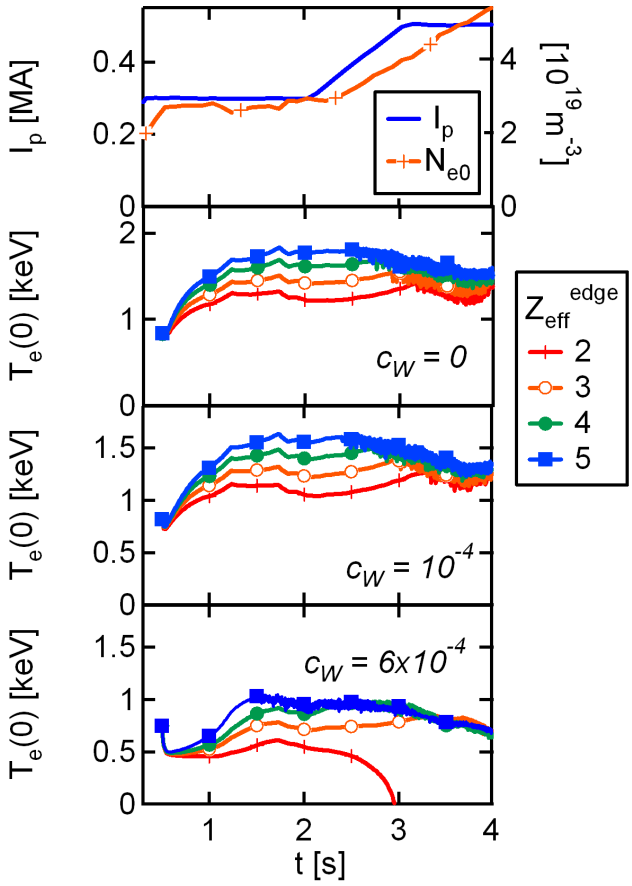

Figure 19. RAPTOR simulations: time evolution of the prescribed plasma current and central electron density (top), and of the predicted central electron temperature without Tungsten, and with a relative fraction of 10^{-4} and 6×10^{-4}, for different values of the edge Z_{eff} with $Z_{eff} = 2 + Z_{eff}^{edge}(r/a)^2$.

radiation. As a result, the cumulative net heat source is unchanged in the plasma core and slightly lowered outside $r/a = 0.5$. Beside this minor modification of the heat flux, the normalized gradient increases significantly. This increase of R/L_{Te} is consistent with the modification of the shear parameter s/q that is known to influence the ITG/TEM threshold [48]. The dilution effect that goes with the increased Z_{eff} contributes to this improvement of the confinement. The relative contributions of both equilibrium and dilution effects is investigated by stand-alone computations with Qualikiz performed from the RAPTOR simulation at $Z_{eff}^{edge} = 2$ (no Nitrogen injection). We perform scans in s/q and in the relative Nitrogen concentration c_N, with a range corresponding to the extreme cases $Z_{eff}^{edge} = 2$ and $Z_{eff}^{edge} = 6$. The results shown in figure 21 evidence the fact that both effects contribute to the reduction of ion diffusivity, while electron diffusivity is weakly sensitive. The increase of core temperature is therefore due to decrease of the

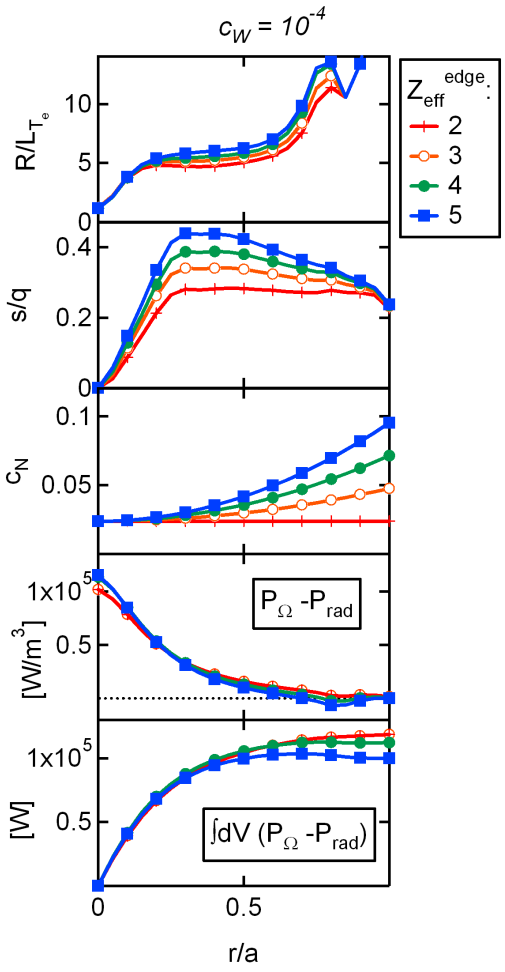

Figure 20. RAPTOR simulations: normalized electron temperature gradient R/L_{Te}, s/q parameter, Nitrogen concentration $c_N = n_N/n_e$, net power density and net cumulative heat source profiles at $t = 2$s, for a Tungsten concentration $c_W = 10^{-4}$.

turbulent transport in a broad region of the plasma extending outside $r/a \approx 0.2$, where dilution and equilibrium modification both play an important role.

If the Tungsten content was larger (we consider here a concentration $c_W = 4\times10^{-4}$), the mechanism would include as well a significant change of the net heat source, as shown in figure 22 : the ohmic heat source in the core is largely increased as the edge Z_{eff} is increased and the net cumulative heat source is more than doubled at mid-radius for $Z_{eff}^{edge} = 5$, thus increasing the robustness towards Tungsten radiation. The increase of the normalized gradient is associated with the combined effect of this larger heat flux as well as with the stabilization of ITG-TEM turbulence due to the increase of s/q and to dilution effect.

Finally, in order to evaluate the sensitivity of the equilibrium profile to resistive MHD mode triggering, we have computed the stability parameter $r\Delta'$ for the $(3,1)$ and $(2,1)$ tearing modes, by solving the tearing equation in cylindrical geometry [49]

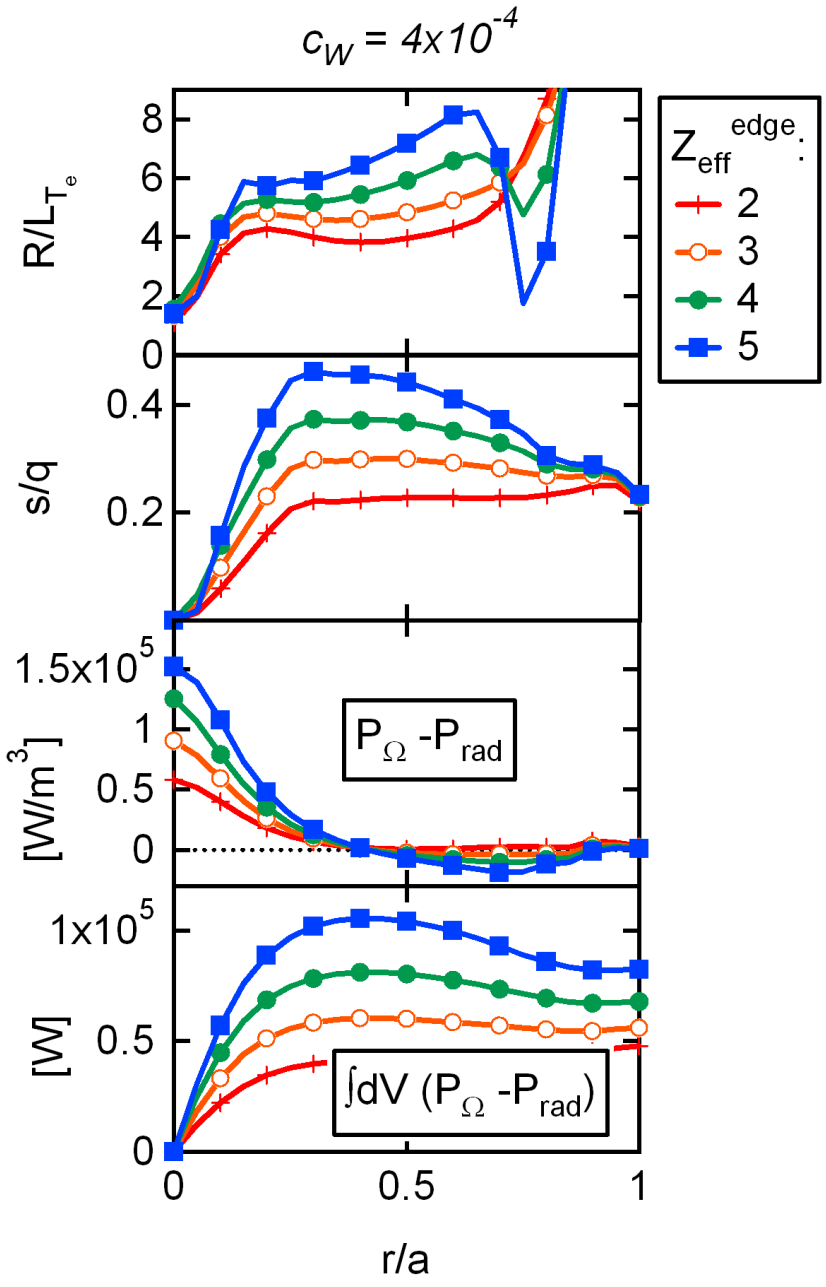

Figure 21. Electron and ion heat diffusivities from stand-alone Qualikiz simulations at $r/a = 0.3$ and $r/a = 0.6$ from the $Z_{eff}^{edge} = 4$ RAPTOR run at $t = 2$s, for a Tungsten concentration $c_W = 10^{-4}$: scan in s/q (left plots) and in c_N (right plots) for a range corresponding to the scan $Z_{eff}^{edge} \in [2, 6]$.

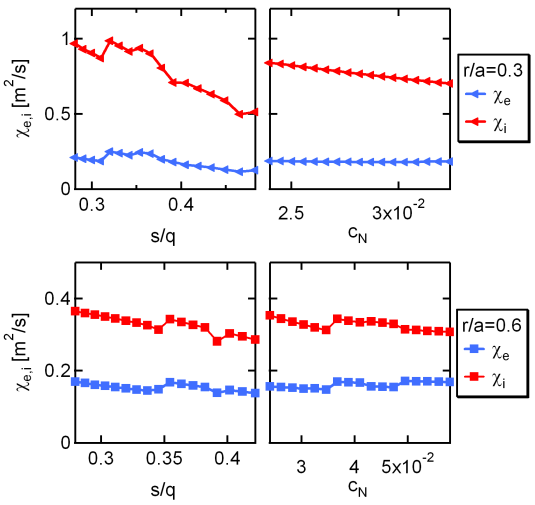

Figure 22. RAPTOR simulations: normalized electron temperature gradient R/L_{Te}, s/q parameter, net power density and net cumulative heat source profiles at $t = 2$s, for a Tungsten concentration $c_W = 4 \times 10^{-4}$.

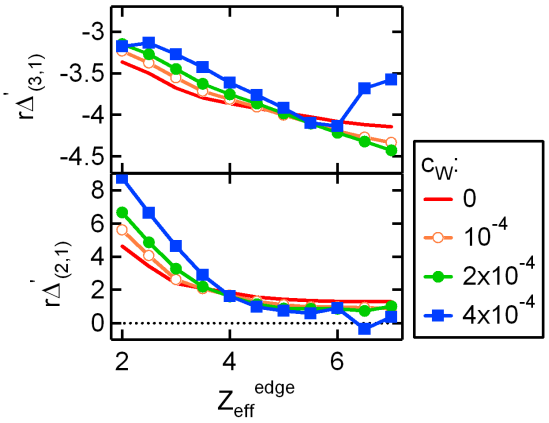

Figure 23. RAPTOR simulations: $(3,1)$ and $(2,1)$ tearing mode stability at $t = 2$s as a function of the edge Z_{eff} for different Tungsten concentrations.

(toroidal effects are therefore ignored in this simple evaluation). As shown in figure 23, the peaking of the current profile stabilizes both islands, supporting experimental observation that MHD stability is improved when applying Nitrogen injection.

5. Discussion

The RAPTOR integrated simulations reported above provide a convincing explanation of the higher core temperature obtained by injecting Nitrogen in the ramp-up phase. The results summarized in figure 16 show that we have a good qualitative agreement on the main key physical plasma parameters. Still, several points remain to be clarified

and motivate further investigations with a more complete physical model. The possible missing ingredients that could be considered for future studies are listed below:

- The first issue encountered in the integrated simulations concerns the edge region, where the turbulent transport was found to be underestimated (figure 15), thus imposing the choice of a boundary at $r/a = 0.8$. This discrepancy could point towards resistive instabilities not accounted for in the QLK model. The value of the temperature at $r/a = 0.8$ strongly impacts all the simulation domain inside, in particular in the present study with variable Nitrogen concentration. This is evidenced in figure 24 where the temperature at $r/a = 0.8$ is varied (here $c_W = 10^{-4}$ and the sawtooth model is not used): without Nitrogen seeding, the core temperature is weakly sensitive to this boundary condition, but the effect is quite strong in the simulations with $Z_{eff}^{edge} = 5$. A higher temperature at $r/a = 0.8$ reduces the impact of Nitrogen injection because of two complementary effects. First, the radiated power density in the edge region is less important because of the cooling factor being lower and the increasing presence of fully stripped Nitrogen ions, and this leads to a lower current profile peaking. The reduction of the s/q parameter destabilizes ITG/TEM turbulence and leads to lower R/L_{Te}. At the same time, the net heat source in the plasma core is decreased: the increase of the plasma resistivity due to lower temperature is not sufficient to compensate for the lower current density in the core, leading to a lower ohmic heat source. A similar observation can be made for the sensitivity to the electron density at $r/a = 0.8$ (figure 25). For this scan, we simply multiply the density gradient by a scalar and we keep the same core density. At larger edge density, the radiated power due to Nitrogen increases, and the net power density in the edge becomes negative, forcing a peaking of the current profile. This increases both the turbulent threshold (larger R/L_{Te} and s/q) and the net power density in the plasma core. The variation of the edge density has also more impact on Nitrogen seeded than on non seeded cases. To summarize, the sensitivity of the core response to the boundary condition in the integrated simulation of light impurity seeding experiments means that it is crucial to properly describe turbulent transport in this edge region in a self-consistent manner.
- We have ignored the change of density peaking induced by Nitrogen injection that is evidenced in figure 4 at $t = 2$s. In order to remove this assumption, we would need to model particle transport during this phase. The changes in turbulence levels and electron temperature could drive this modification of density peaking. The scan in the density at $r/a = 0.8$ with fixed core density shown in figure 25 does not go in the direction of enhancing the effect of Nitrogen seeding when reducing the edge density. But it is not excluded that a self-consistent treatment of this issue would yield density profile shapes going in a different direction.
- As an extension of the issue of density peaking, the modeling of the particle source including the neutral population and ionization processes would bring crucial key

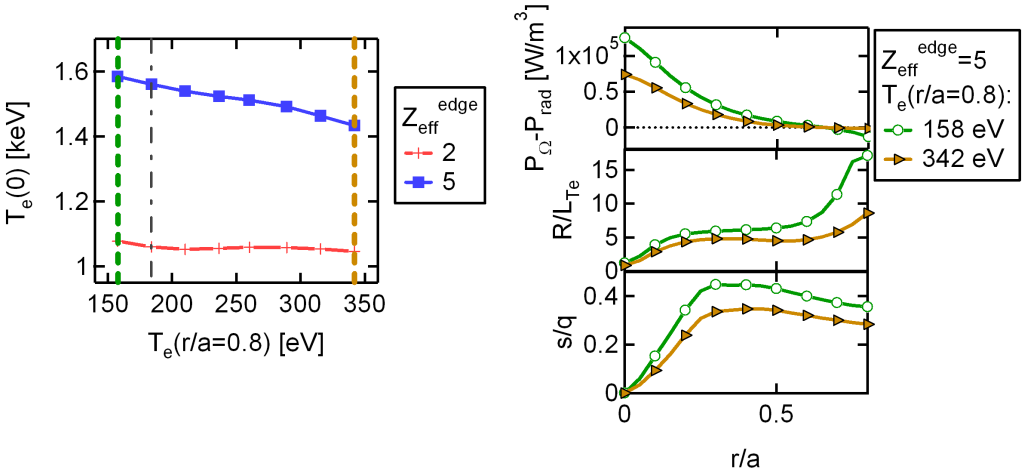

Figure 24. Left: Core electron temperature with ($Z_{eff}^{edge} = 5$) and without ($Z_{eff}^{edge} = 2$) Nitrogen injection, as a function of the temperature prescribed at $r/a = 0.8$. Right: profiles of the net heat source, normalized temperature gradient and s/q at $Z_{eff}^{edge} = 5$ for the lowest and highest temperature at the boundary. The thin vertical line indicates the default value used in this study ($c_W = 10^{-4}$, no sawtooth model).

physical ingredients for the edge plasma dynamics when approaching detachment conditions that are indeed observed here.

- The transport of light and heavy impurities could be modeled in order to obtain a consistent radial distribution of the ohmic source (from light impurities) and radiative losses (from both light and heavy ions) during the current ramp. The cooling factor varies significantly for all ion species in the temperature range that is crossed in this phase, and this is instrumental for properly describing radiative losses. For Tungsten, this cooling factor is not considered to be well established for temperatures below 1 keV [50], thus motivating further fundamental research in this area.

These issues, among others, are still pending for reaching a predictive capability for the plasma ramp-up phase. Meanwhile, dedicated experiments and simplified integrated modeling tools provide a practical path towards the optimization of this crucial phase of a tokamak scenario.

6. Conclusion

In a Tungsten environment, the early plasma phase has to deal with the W burn through which occurs at high electron temperature, around 1.5 keV. Core heating has to win over core cooling to avoid the formation of broad or hollow current profile prone to the triggering of MHD activity. As reported in the present paper, Nitrogen injection during the plasma current ramp-up has been used successfully for solving these issues

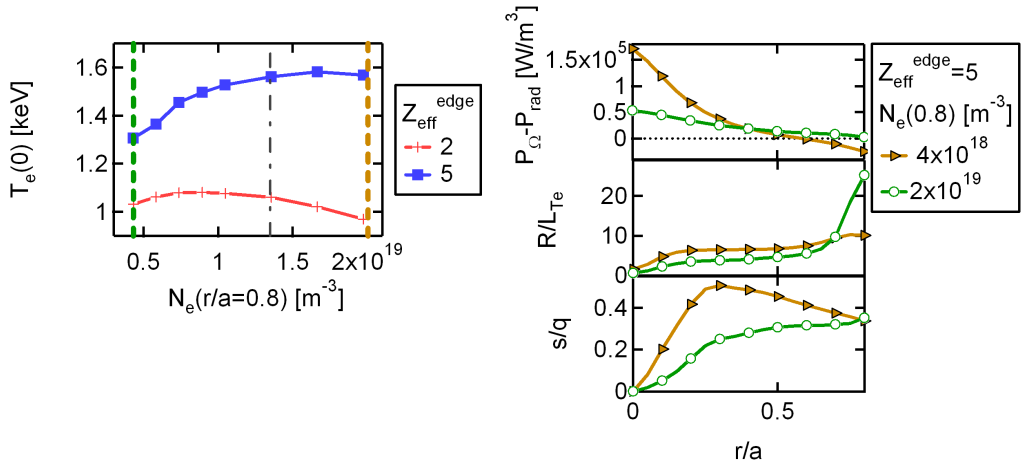

Figure 25. Left: Core electron temperature with ($Z_{eff}^{edge} = 5$) and without ($Z_{eff}^{edge} = 2$) Nitrogen injection, as a function of the density prescribed at $r/a = 0.8$. Right: profiles of the net heat source, normalized temperature gradient and s/q at $Z_{eff}^{edge} = 5$ for the lowest and highest density at the boundary. The thin vertical line indicates the default value used in this study ($c_W = 10^{-4}$, no sawtooth model).

in WEST. This favorable effect has been analyzed with the support of integrated simulations with the RAPTOR code, complemented with the Neural Network version of the quasilinear turbulent transport code QualiKiz. We find that the beneficial effect of Nitrogen injection is obtained thanks to the peaking of the current profile resulting from the combination of edge radiation cooling and improved confinement. These two mechanisms are strongly linked, since the modification of the magnetic equilibrium acts on ITG/TEM turbulence, and modifies temperature as well as plasma resistivity, thus closing the loop with the change of the current profile. The reduction of turbulence with Nitrogen seeding includes as well a dilution effect. We showed also that if Tungsten contamination was large (larger at least than the experiments reported here), a significant increase of ohmic heating in the plasma core would also help peaking the core temperature and the current profile, allowing to compensate for Tungsten radiation, and opening the operational window in this respect. Experimental measurements indicate that N_2 injection induces a transient detachment that cancels Tungsten sputtering in the divertor region, but increases it after re-attachment. This does not induce a noticeable change of core radiation in the current flat top, but the detached phase sets however an upper limit in terms of N_2 injection, since a peripheral radiative layer evidenced by the visible camera finally grows above some injection level, and leads to a loss of plasma control.

Acknowledgments

This work has been carried out within the framework of the French Research Federation for Fusion Studies, and of the EUROfusion Consortium, and it was supported in part

by the Swiss National Science Foundation. It has received funding from the Euratom research and training programme 2014-2018 and 2019-2020 under grant agreement No 633053. The views and opinions expressed herein do not necessarily reflect those of the European Commission.

References

[1] A Kallenbach, M Bernert, R Dux, L Casali, T Eich, L Giannone, A Herrmann, R McDermott, A Mlynek, H W Mller, F Reimold, J Schweinzer, M Sertoli, G Tardini, W Treutterer, E Viezzer, R Wenninger, and M Wischmeier and. Impurity seeding for tokamak power exhaust: from present devices via ITER to DEMO. *Plasma Physics and Controlled Fusion*, 55(12):124041, nov 2013.

[2] D. Post, J. Abdallah, R. E. H. Clark, and N. Putvinskaya. Calculations of energy losses due to atomic processes in tokamaks with applications to the International Thermonuclear Experimental Reactor divertor. *Physics of Plasmas*, 2(6):2328–2336, 1995.

[3] Y. Gribov, D. Humphreys, K. Kajiwara, E.A. Lazarus, J.B. Lister, T. Ozeki, A. Portone, M. Shimada, A.C.C. Sips, and J.C. Wesley. Chapter 8: Plasma operation and control. *Nuclear Fusion*, 47(6):S385, 2007.

[4] R Neu, R Dux, A Geier, A Kallenbach, R Pugno, V Rohde, D Bolshukhin, J C Fuchs, O Gehre, O Gruber, J Hobirk, M Kaufmann, K Krieger, M Laux, C Maggi, H Murmann, J Neuhauser, F Ryter, A C C Sips, A Stbler, J Stober, W Suttrop, H Zohm, and the ASDEX Upgrade Team. Impurity behaviour in the ASDEX upgrade divertor tokamak with large area tungsten walls. *Plasma Physics and Controlled Fusion*, 44(6):811–826, may 2002.

[5] F Alladio, M L Apicella, G Apruzzese, E Bartiromo, O Borra, G Bracco, G Buceti, P Buratti, C Centioli, M Ciotti, V Cocilovo, I Condrea, F Crisanti, R DeAngelis, B Esposito, C Ferro, G Franzoni, D Frigione, L Gabellieri, E Giovannozzi, G Granucci, M Grolli, A Imparato, H Kroegler, M Leigheb, L Lovisetto, G Maddaluno, G Mazzitelli, P Micozzi, A Moleti, F Orsitto, L Panaccione, D Pacella, M Panella, V Pericoli, L Pieroni, S Podda, G B Righetti, F Romanelli, S E Segre, E Sternini, A A Tuccillo, O Tudisco, F Valente, V Vitale, R Zagorski, V Zanza, and M Zerbini. Plasma characteristics in FTU with different plasma facing materials. *Plasma Physics and Controlled Fusion*, 36(12B):B253–B261, dec 1994.

[6] J Rapp, M Z Tokar, L Knen, H R Koslowski, G Bertschinger, M Brix, H Claassen, R Jaspers, A Krmer-Flecken, K Ohya, V Philipps, A Pospieszczyk, U Samm, T Tanabe, G Telesca, B Unterberg, and G Van Oost. Transport studies of high-Z elements in Neon edge radiation cooled discharges in TEXTOR-94. *Plasma Physics and Controlled Fusion*, 39(10):1615–1634, oct 1997.

[7] P Buratti, F Alladio, P Micozzi, O Tudisco, L Acitelli, B Angelini, M L Apicella, G Apruzzese, E Barbato, A Bertocchi, G Bracco, A Bruschi, G Buceti, A Cardinali, C Centioli, R Cesario, S Ciattaglia, M Ciotti, S Cirant, V Cocilovo, F Crisanti, R De Angelis, F De Marco, B Esposito, D Frigione, L Gabellieri, G Gatti, E Giovannozzi, C Gourlan, G Granucci, M Grolli, A Imparato, H Kroegler, M Leigheb, L Lovisetto, G Maddaluno, G Maffia, A Mancuso, M Marinucci, G Mazzitelli, F Mirizzi, F P Orsitto, D Pacella, L Panaccione, M Panella, V Pericoli Ridolfini, L Pieroni, S Podda, G B Righetti, F Romanelli, F Santini, M Sassi, S E Segre, A Simonetto, C Sozzi, S Sternini, A A Tuccillo, F Valente, V Vitale, G Vlad, V Zanza, and M Zerbini. MHD activity in FTU plasmas with reversed magnetic shear. *Plasma Physics and Controlled Fusion*, 39(12B):B383–B394, dec 1997.

[8] B. Carreras, H.R.Hicks, and B.V. Waddell. Tearing-mode activity for hollow current profiles. *Nuclear Fusion*, 19(5):583–596, 1979.

[9] C. Bourdelle, J.F. Artaud, V. Basiuk, M. Bécoulet, S. Brémond, J. Bucalossi, H. Bufferand, G. Ciraolo, L. Colas, Y. Corre, X. Courtois, J. Decker, L. Delpech, P. Devynck, G. Dif-Pradalier,

R.P. Doerner, D. Douai, R. Dumont, A. Ekedahl, N. Fedorczak, C. Fenzi, M. Firdaouss, J. Garcia, P. Ghendrih, C. Gil, G. Giruzzi, M. Goniche, C. Grisolia, A. Grosman, D. Guilhem, R. Guirlet, J. Gunn, P. Hennequin, J. Hillairet, T. Hoang, F. Imbeaux, I. Ivanova-Stanik, E. Joffrin, A. Kallenbach, J. Linke, T. Loarer, P. Lotte, P. Maget, Y. Marandet, M.L. Mayoral, O. Meyer, M. Missirlian, P. Mollard, P. Monier-Garbet, P. Moreau, E. Nardon, B. Pégourié, Y. Peysson, R. Sabot, F. Saint-Laurent, M. Schneider, J.M. Travère, E. Tsitrone, S. Vartanian, L. Vermare, M. Yoshida, and R. Zagorski and. WEST physics basis. *Nuclear Fusion*, 55(6):063017, may 2015.

[10] E.A. Lazarus, J.D. Bell, C.E. Bush, A. Carnevali, B.A. Carreras, W.H. Casson, J.L. Dunlap, P.H. Edmonds, A.C. England, W. L. Gardner, G.A. Hallock, J.T. Hogan, H.C. Howe, D.P. Hutchinson, R.R. Kindsfather, R.C. Isler, R.A. Langley, C.H. Ma, J. Mathew, P.K. Mioduszewski, M. Murakami, G.H. Neilson, V.K. Pare, D.J. Sigmar, C.E. Thomas, R.M. Wieland, J.B. Wilgen, W.R. Wing, A.J. Wootton, and K.E. Yokoyama. Confinement in beam-heated plasmas: the effects of low-Z impurities. *Nuclear Fusion*, 25(2):135–149, feb 1985.

[11] A.M Messiaen, J Ongena, U Samm, B Unterberg, P.E Vandenplas, G. Van Oost, G. Van Wassenhove, J Winter, D Boucher, P Dumortier, F Durodie, H.G Esser, H Euringer, B Giesen, E Hintz, M Lochter, M.Z Tokar, G.H Wolf, G Fuchs, D.L Hillis, F Hoenen, P Huttemann, R Koch, L Konen, H.R Koslowski, A Kramer-Flecken, D Pettiaux, A Pospieszczyk, B Schweer, H Soltwisch, G Telesca, R Uhlemann, R. van Nieuwenhove, M Vervier, G Waidmann, and R.R Weynants. Improved confinement with edge radiative cooling at high densities and high heating power in TEXTOR. *Nuclear Fusion*, 34(6):825–836, jun 1994.

[12] O. Gruber, A. Kallenbach, M. Kaufmann, K. Lackner, V. Mertens, J. Neuhauser, F. Ryter, H. Zohm, M. Bessenrodt-Weberpals, K. Büchl, S. Fiedler, A. Field, Ch. Fuchs, C. Garcia-Rosales, G. Haas, A. Herrmann, W. Herrmann, S. Hirsch, W. Köppendörfer, P. Lang, G. Lieder, K.-F. Mast, C. S. Pitcher, M. Schittenhelm, J. Stober, W. Suttrop, M. Troppmann, M. Weinlich, M. Albrecht, M. Alexander, K. Asmussen, M. Ballico, K. Behler, K. Behringer, H. S. Bosch, M. Brambilla, A. Carlson, D. Coster, L. Cupido, H. J. DeBlank, S. De Pena Hempel, S. Deschka, C. Dorn, R. Drube, R. Dux, A. Eberhagen, W. Engelhardt, H.-U. Fahrbach, H.-U. Feist, D. Fieg, G. Fußmann, O. Gehre, J. Gernhardt, P. Ignacz, B. Jüttner, W. Junker, T. Kass, K. Kiemer, H. Kollotzek, M. Kornherr, K. Krieger, B. Kurzan, R. Lang, M. Laux, M. E. Manso, M. Maraschek, H.-M. Mayer, P. McCarthy, D. Meisel, R. Merkel, H. Murmann, B. Napiontek, D. Naujoks, G. Neu, R. Neu, J.-M. Noterdaeme, G. Pautasso, W. Poschenrieder, G. Raupp, H. Richter, T. Richter, H. Röhr, J. Roth, N. Salmon, H. Salzmann, W. Sandmann, H.-B. Schilling, H. Schneider, R. Schneider, W. Schneider, K. Schönmann, G. Schramm, U. Schumacher, J. Schweinzer, U. Seidel, F. Serra, A. Silva, M. Sokoll, E. Speth, A. Stäbler, K.-H. Steuer, B. Streibl, W. Treutterer, M. Ulrich, P. Varela, H. Vernickel, O. Vollmer, H. Wedler, U. Wenzel, F. Wesner, R. Wunderlich, D. Zasche, and H. P. Zehrfeld. Observation of Continuous Divertor Detachment in H-Mode Discharges in ASDEX Upgrade. *Phys. Rev. Lett.*, 74:4217–4220, May 1995.

[13] Unterbarg B., Samm U. et Tokar M.Z., Messiaen A.M., Ongena J., and Jaspers R. The Radiative Improved Mode in TEXTOR: power exhaust and improved confinement at high density. *Fusion Sience and Technology*, 47:187, 2005.

[14] A. Kallenbach, M. Balden, R. Dux, T. Eich, C. Giroud, A. Huber, G.P. Maddison, M. Mayer, K. McCormick, R. Neu, T.W. Petrie, T. Ptterich, J. Rapp, M.L. Reinke, K. Schmid, J. Schweinzer, and S. Wolfe. Plasma surface interactions in impurity seeded plasmas. *Journal of Nuclear Materials*, 415(1, Supplement):S19 – S26, 2011. Proceedings of the 19th International Conference on Plasma-Surface Interactions in Controlled Fusion.

[15] N. Bonanomi, P. Mantica, J. Citrin, C. Giroud, E. Lerche, C. Sozzi, D. Taylor, M. Tsalas, and D. Van Eester and. Effects of nitrogen seeding on core ion thermal transport in JET ILW l-mode plasmas. *Nuclear Fusion*, 58(2):026028, jan 2018.

[16] X. Yang, P. Manas, C. Bourdelle, J. F. Artaud, R. Sabot, Y. Camenen, J. Citrin, F. Clairet,

C. Desgranges, P. Devynck, T. Dittmar, A. Ekedahl, N. Fedorczak, C. Gil, T. Loarer, Ph. Lotte, O. Meyer, J. Morales, M. Peret, Y. Peysson, C. D. Stephens, G. Urbanczyk, D. Vézinet, L. Zhang, and X. Gong. Core tungsten transport in WEST long pulse l-mode plasmas. *Nuclear Fusion*, 60(8):086012, jul 2020.

[17] R. Dux, V. Bobkov, A. Herrmann, A. Janzer, A. Kallenbach, R. Neu, M. Mayer, H.W. Mller, R. Pugno, T. Ptterich, V. Rohde, and A.C.C. Sips. Plasma-wall interaction and plasma behaviour in the non-boronised all tungsten asdex upgrade. *Journal of Nuclear Materials*, 390-391:858 – 863, 2009. Proceedings of the 18th International Conference on Plasma-Surface Interactions in Controlled Fusion Device.

[18] P Dumortier, P Andrew, G Bonheure, R V Budny, R Buttery, M Charlet, I Coffey, M de Baar, P C de Vries, T Eich, D Hillis, C Ingesson, S Jachmich, G Jackson, A Kallenbach, H R Koslowski, K D Lawson, C Liu, G Maddison, A M Messiaen, P Monier-Garbet, M Murakami, M F F Nave, J Ongena, V Parail, M E Puiatti, J Rapp, F Sartori, M Stamp, J D Strachan, W Suttrop, G Telesca, M Tokar, B Unterberg, M Valisa, M von Hellermann, B Weyssow, and contributors to the EFDA-JET Workprogramme. Confinement properties of high density impurity seeded ELMy h-mode discharges at low and high triangularity on JET. *Plasma Physics and Controlled Fusion*, 44(9):1845–1861, aug 2002.

[19] P Monier-Garbet, Ph Andrew, P Belo, G Bonheure, Y Corre, K Crombe, P Dumortier, T Eich, R Felton, J Harling, J Hogan, A Huber, S Jachmich, E Joffrin, H.R Koslowski, A Kreter, G Maddison, G.F Matthews, A Messiaen, M.F Nave, J Ongena, V Parail, M.E Puiatti, J Rapp, R Sartori, J Stober, M.Z Tokar, B Unterberg, M Valisa, I Voitsekhovitch, M. von Hellermann, and JET-EFDA contributors. Impurity-seeded ELMy h-modes in JET, with high density and reduced heat load. *Nuclear Fusion*, 45(11):1404–1410, oct 2005.

[20] Y. Marandet, I. Ivanova-Stanik, R. Zagrski, C. Bourdelle, J. Bucalossi, H. Bufferand, G. Ciraolo, and E. Tsitrone. Self-Consistent COREDIV Modelling of WEST Plasma Scenarios. *Contributions to Plasma Physics*, 54(4-6):353–357, 2014.

[21] N. Fedorczak, P. Monier-Garbet, T. Pütterich, S. Brezinsek, P. Devynck, R. Dumont, M. Goniche, E. Joffrin, E. Lerche, B. Lipschultz, E. de la Luna, G. Maddison, C. Maggi, G. Matthews, I. Nunes, F. Rimini, E.R. Solano, P. Tamain, M. Tsalas, and P. de Vries. Tungsten transport and sources control in JET ITER-like wall H-mode plasmas. *Journal of Nuclear Materials*, 463:85 – 90, 2015. PLASMA-SURFACE INTERACTIONS 21.

[22] C.D. Challis, S. Brezinsek, I.H. Coffey, M. Fontana, N.C. Hawkes, D.L. Keeling, D.B. King, G. Pucella, and E. Viezzer. Effect of fuel isotope mass on q-profile formation in JET hybrid plasmas. *Nuclear Fusion*, 60(8):086008, jul 2020.

[23] M. Oberkofler, D. Douai, S. Brezinsek, J.W. Coenen, T. Dittmar, A. Drenik, S.G. Romanelli, E. Joffrin, K. McCormick, M. Brix, G. Calabro, M. Clever, C. Giroud, U. Kruezi, K. Lawson, Ch. Linsmeier, A. Martin Rojo, A. Meigs, S. Marsen, R. Neu, M. Reinelt, B. Sieglin, G. Sips, M. Stamp, and F.L. Tabares. First nitrogen-seeding experiments in JET with the ITER-like Wall. *Journal of Nuclear Materials*, 438:S258–S261, 2013. Proceedings of the 20th International Conference on Plasma-Surface Interactions in Controlled Fusion Devices.

[24] A. Drenik, L. Laguardia, R. McDermott, G. Meisl, R. Neu, M. Oberkofler, E. Pawelec, R.A. Pitts, S. Potzel, T. Ptterich, T. Reichbauer, V. Rohde, M. Seibt, G. De Temmerman, R. Zaplotnik, and and. Evolution of nitrogen concentration and ammonia production in N2-seeded H-mode discharges at ASDEX Upgrade. *Nuclear Fusion*, 59(4):046010, feb 2019.

[25] T Dittmar, T Loarer, A Drenik, C Bourdelle, S Brezinsek, C Desgranges, D Douai, N Fedorczak, R Guirlet, J Gunn, O Meyer, L Laguardia, and E Tsitrone and. Long pulse d2 and n2 seeded discharges on the upper actively cooled tungsten divertor of WEST. *Physica Scripta*, T171:014074, jan 2020.

[26] T. Loarer, T. Dittmar, E. Tsitrone, R. Bisson, C. Bourdelle, S. Brezinsek, J. Bucalossi, Y. Corre, L. Delpech, C. Desgranges, G. De Temmerman, D. Douai, A. Ekedahl, N. Fedorczak, A. Gallo, J. Gaspar, J. Gunn, M. Houry, P. Maget, R. Mitteau, and P. Moreau and. Long discharges in a

steady state with D2 and N2 on the actively cooled tungsten upper divertor in WEST. *Nuclear Fusion*, 60(12):126046, oct 2020.

[27] F. Felici, O. Sauter, S. Coda, B.P. Duval, T.P. Goodman, J-M. Moret, and J.I. Paley and. Real-time physics-model-based simulation of the current density profile in tokamak plasmas. *Nuclear Fusion*, 51(8):083052, aug 2011.

[28] F Felici and O Sauter. Non-linear model-based optimization of actuator trajectories for tokamak plasma profile control. *Plasma Physics and Controlled Fusion*, 54(2):025002, jan 2012.

[29] J. L. Ségui, D. Molina, G. Giruzzi, M. Goniche, G. Huysmans, P. Maget, and M. Ottaviani Tore Supra Team. An upgraded 32-channel heterodyne electron cyclotron emission radiometer on Tore Supra. *Review of Scientific Instruments*, 76(12):123501, 2005.

[30] Pascal Devynck, Nicolas Fedorczak, Rui Mao, and Stephane Vartanian. Calculation of the radiated power in WEST. *Journal of Physics Communications*, 2021.

[31] Pascal Devynck. in preparation. 2021.

[32] O. Meyer, O. M. Jones, J. C. Giacalone, J. Y. Pascal, D. Raulin, H. Xu, M. H. Aumeunier, R. Baude, A. Escarguel, C. Gil, J. H. Harris, J.-C. Hatchressian, C. C. Klepper, S. Larroque, Ph. Lotte, Ph. Moreau, B. Pgouri, and S. Vartanian. Development of visible spectroscopy diagnostics for W sources assessment in WEST. *Review of Scientific Instruments*, 87(11):11E309, 2016.

[33] R. Guirlet, I. Song, G. Moureau, T. Batal, J.L. Schwob, C. Seon, C. Desgranges, S. Vartanian, H. Shin, and W. Choe. Extreme UV spectrometers for the tungsten 40 - 70 Åemission in the WEST tokamak. *Journal of Instrumentation*, 14(10):C10036–C10036, oct 2019.

[34] R. Dejarnac, D. Sestak, J.P. Gunn, M. Firdaouss, H. Greuner, J-Y. Pascal, M. Richou, and H. Roche. Flush-mounted langmuir probes in the west tokamak divertor. *Fusion Engineering and Design*, 163:112120, 2021.

[35] Blaise Faugeras. An overview of the numerical methods for tokamak plasma equilibrium computation implemented in the NICE code. *Fusion Engineering and Design*, 160:112020, 2020.

[36] O Février, C Theiler, J R Harrison, C K Tsui, K Verhaegh, C Wthrich, J A Boedo, H De Oliveira, B P Duval, B Labit, B Lipschultz, R Maurizio, H Reimerdes, and and. Nitrogen-seeded divertor detachment in TCV L-mode plasmas. *Plasma Physics and Controlled Fusion*, 62(3):035017, feb 2020.

[37] Y. Marandet, H. Bufferand, J. Bucalossi, G. Ciraolo, S.W. Lisgo, and E. Tsitrone. Assessment of tungsten sources in the edge plasma of WEST. *Journal of Nuclear Materials*, 463:629 – 633, 2015. PLASMA-SURFACE INTERACTIONS 21.

[38] C. Bourdelle, X. Garbet, F. Imbeaux, A. Casati, N. Dubuit, R. Guirlet, and T. Parisot. A new gyrokinetic quasilinear transport model applied to particle transport in tokamak plasmas. *Physics of Plasmas*, 14(11):112501, 2007.

[39] K. L. van de Plassche, J. Citrin, C. Bourdelle, Y. Camenen, F. J. Casson, V. I. Dagnelie, F. Felici, A. Ho, and S. Van Mulders. Fast modeling of turbulent transport in fusion plasmas using neural networks. *Physics of Plasmas*, 27(2):022310, 2020.

[40] F. Felici, J. Citrin, A.A. Teplukhina, J. Redondo, C. Bourdelle, F. Imbeaux, O. Sauter, JET Contributors, and the EUROfusion MST1 Team. Real-time-capable prediction of temperature and density profiles in a tokamak using RAPTOR and a first-principle-based transport model. *Nuclear Fusion*, 58(9):096006, jul 2018.

[41] For information on the Atomic Data and Analysis Structure (ADAS). http://www.adas.ac.uk/.

[42] T Pütterich, R Neu, R Dux, A D Whiteford, M G O´Mullane, and the ASDEX Upgrade Team. Modelling of measured tungsten spectra from ASDEX upgrade and predictions for ITER. *Plasma Physics and Controlled Fusion*, 50(8):085016, jun 2008.

[43] F Porcelli, D Boucher, and M N Rosenbluth. Model for the sawtooth period and amplitude. *Plasma Physics and Controlled Fusion*, 38(12):2163, 1996.

[44] Chiara Piron, Gabriele Manduchi, Paolo Bettini, Federico Felici, Claudio Finotti, Paolo Franz, Ondrej Kudlacek, Giuseppe Marchiori, Lionello Marrelli, J.-M. Moret, Paolo Piovesan, Olivier Sauter, and Cesare Taliercio. Integration of the state observer RAPTOR in the real-time MARTe

framework at RFX-mod. *Fusion Engineering and Design*, 123:616 – 619, 2017. Proceedings of the 29th Symposium on Fusion Technology (SOFT-29) Prague, Czech Republic, September 5-9, 2016.

[45] G.V. Pereverzev and Y.P. Yushmanov. ASTRA Automated System for Transport Analysis in a tokamak . *IPP - Technical Report*, (5/42), 2002.

[46] J. E. Kinsey, G. M. Staebler, and R. E. Waltz. The first transport code simulations using the trapped gyro-landau-fluid model. *Physics of Plasmas*, 15(5):055908, 2008.

[47] A.G. Peeters, Y. Camenen, F.J. Casson, W.A. Hornsby, A.P. Snodin, D. Strintzi, and G. Szepesi. The nonlinear gyro-kinetic flux tube code GKW. *Computer Physics Communications*, 180(12):2650 – 2672, 2009. 40 YEARS OF CPC: A celebratory issue focused on quality software for high performance, grid and novel computing architectures.

[48] C Fourment, G T Hoang, L-G Eriksson, X Garbet, X Litaudon, and G Tresset. Role of the current density profile on drift wave stability in internal transport barrier reversed magnetic shear experiments at JET and tore supra. *Plasma Physics and Controlled Fusion*, 45(3):233–250, feb 2003.

[49] J. Wesson. *Tokamaks*. Oxford Science Publications, 1997.

[50] T Pütterich, E Fable, R Dux, M OMullane, R Neu, M Siccinio, the ASDEX Upgrade Team, and JET EFDA Contributors. Determination of the tolerable impurity concentrations in a fusion reactor using a consistent set of cooling factors. *Nuclear Fusion*, 59:056013, nov 2019.